Volume 1 | Number 1 | Jan 2013 | Pages 1–100

Nanoscale

www.rsc.org/nanoscale

ROYAL SOCIETY OF CHEMISTRY

ROYAL SOCIETY OF CHEMISTRY

www.rsc.org/nanoscale

Please do not adjust margins

Nanoscale

Journal Name

ARTICLE

A core/shell/satellite anticancer platform for 808 NIR Light-Driven multimodal imaging and combined chemo-/photothermal therapy

Guixin Yang,[a] Ruichan Lv,[a] Fei He,[a] Fengyu Qu[b],*, Shili Gai,[a] Shaokang Du,[a] Zibo Wei[a] and Piaoping Yang[a],*

In this contribution, a novel multifunctional anti-cancer nanoplatform has been firstly constructed by conjugating photothermal agent (CuS nanoparticles) and cancer cell target agent (folic acid, FA) onto the surface of mesoporous silica coated core-shell-shell up-conversion nanoparticles (UCNPs). It was found that the doxorubicin (DOX) loaded system exhibits obviously pH and NIR-responsive release behaviour and the drug can be targetedly delivered into the cancer cells by receptor mediated endocytosis manner. Furthermore, both photothermal therapy (PTT) and chemotherapy can be triggered simultaneously by a single 808 nm near infrared (NIR) light, thus leading to a synergistic effect. The combined chemo- and NIR photothermal therapy can significantly improve the therapeutic efficacy superior to any single therapy, which has been evidenced by both *in vitro* and *in vivo* results. Besides, due to the doped rare earth ions, the platform also exhibits good up-conversion luminescence (UCL), computed tomography (CT) and magnetic resonance imaging (MRI) properties. Based on the excellent multimodal imaging and anti-tumor properties, the multifunctional nanoplatform should be a promising candidate for imaging-guided anti-cancer therapy.

Introduction

Nowadays, design and synthesis of hybrid composite that combines multiple nanomaterials with functional properties have attracted more and more interest for simultaneous diagnosis[1,2] and therapy of diseases.[3–7] Several therapy techniques have been developed for cancer therapy, such as radiotherapy,[8–11] photo-thermal therapy[12–16] and chemotherapy.[17–19] For instance, radiotherapy (RT) uses high energy, highly focused radiation rays (generally x-ray and γ-ray) as virtual "knives" to kill cancer cells, but it is still difficult to restrict their penetration depth in tissues. Chemotherapy provides an efficient drug but suffers from the limitation of severe side effects and drug resistance.[20,21] Therefore, taking advantage of modality therapy together should satisfy the meeting of the therapeutic process and medical research.

Recently, the lanthanide-doped up-conversion core-shell structured composites combined with mesoporous silica have been a research hotpot among the materials science,[22–27] because this kind of composite possesses the advantages of

UCNPs and mesoporous structure. The UCNPs can emit higher-energy visible photons after being excited by lower-energy near-infrared (NIR) photons.[28–38] In particular, the utilization of NIR light rather than ultraviolet light as the excitation source has the merits of low photo-damage, low background fluorescence, and deep penetration into biological tissue.[39–42] Meanwhile, the mesoporous silica owns high surface area, suitable mesoporous pore size, easily modified surface and high biocompatibility, which can be used as diverse anti-cancers' drug carriers.[43–47] However, the conventional 980 nm NIR laser used as an excitation source for biological applications usually causes serious overheating to cell and tissue due to the high absorbance of water at 980 nm.[48–50] Moreover, the intensity of the 980 nm NIR laser will be markedly decreased when diffusing in the biological tissues, leading to the limited penetration depth. Therefore, it is necessary to shift the excitation wavelength into an appropriate range in the medical spectral window (700-900 nm), where the biological tissues have the minimal adsorption, thus achieving high penetration depth.

Very recently, Yao and co-workers reported Nd^{3+}-sensitized UC process upon 808 nm excitation.[51] In the core-shell-shell structure, the successive energy transfer from Nd^{3+} to Yb^{3+} then to activator leads to a maximum UC emission intensity by shielding the energy transfer back from activators to Nd3+. Another work showed that Nd^{3+}-sensitized core-shell structured nanoparticles can achieve high UC efficiency upon 808 nm NIR laser excitation, which could trigger the photosensitizer to generate reactive oxygen series (ROS) thus to kill tumor cells for photodynamic therapy.[52] However, most

[a] *Key Laboratory of Superlight Materials and Surface Technology, Ministry of Education, College of Material Sciences and Chemical Engineering, Harbin Engineering University, Harbin, 150001, P. R. China. E-mail: yangpiaoping@hrbeu.edu.cn*
[b] *Key Laboratory for Photonic and Electronic Bandgap Materials, Ministry of Education, College of Chemistry and Chemical Engineering, Harbin Normal University, Harbin, 150025, P. R. China. E-mail: qufengyu2013@gmail.com*
Electronic Supplementary Information (ESI) available: XRD patterns of the samples, XRD and TEM image of CuS NPs, N_2 adsorption/desorption isotherm and pore size distribution of UCMSNs, FT-IR spectra and UC emission spectra of the samples, and T_1-weighted MR images of UCMSNs. See DOI: 10.1039/x0xx00000x

of works about the Nd^{3+}-sensitized UCNPs focused on the construction of diverse structure and some for the photodymanic therapy,[53–56] while UCNPs for photothermal therapy induced by a 808 nm NIR light has never been reported so far.

Currently, photothermal nanoparticles with strong absorbance of NIR laser have been extensively explored to increase the photothermal conversion efficiency and correspondingly enhance the thermal lethality in subcutaneous tumors.[57–64] Compared with conventional Au or Ag nanoparticles, metal sulfide nanoparticles (NPs) are more and more popular due to the low cost and high biocompatibility.[65] Moreover, because the maximum NIR absorption of Au nanoparticles derived from the surface plasmon resonance (SPR) is dependent on the dielectric constant of the surrounding matrix, the PTT efficiency is affected greatly by the surroundings. For comparison, the NIR light absorption of metal sulfide nanoparticles based on the d-d energy band transition of metal ions instead of SPR cannot be affected by the surrounding circumstance, thus leading to higher photothermal ablation efficiency and better thermal stability in anti-cancer therapy *in vivo*.[14,64] Hence, the combination of metal sulfide nanoparticles in a functional system for multimodal therapy should be highly potential for cancer therapy.

Herein, we conjugated CuS nanoparticles onto the mesoporous silica coated core-shell-shell structured $NaGdF_4$:Yb,Er@$NaGdF_4$:Yb@$NaNdF_4$:Yb for simultaneous multi-modal imaging and combined chemo- and photothermal therapies. The attached CuS nanoparticles can induce obvious thermal effect upon NIR laser irradiation, resulting in an obvious photothermal anti-cancer therapy. What's more, the higher absorbance of CuS nanocrystals at 808 nm can enhance the efficiency to reduce the laser power for treatment and deeper penetration depth in biological tissues. Besides, CuS nanocrystals have demonstrated to be a low long-time toxicity and can be biodegradable. Meanwhile, the release of loaded anti-cancer drug (DOX) can be apparently enhanced by the thermal effect, resulting in a synergistic therapeutic effect. Simultaneously, the multimodal bioimaging properties of the as-synthesized platform have also been investigated *in vitro* and *in vivo* in detail. To the best of our knowledge, we developed a new type of photo thermal anti-tumor platform based on this kind of core-shell-shell nanostructures that convert 808 nm NIR light for its multimodal imaging and synergistic therapy, which may pave the way for the further applications of such nanoparticle-based nanotheranostic.

Results and discussion

Synthesis and characterization of the samples. The schematic procedure for the synthesis of UCMSNS is illustrated in Scheme 1. Firstly, $NaGdF_4$:Yb,Er core was obtained by a thermal decomposition method. Then, the active shell $NaGdF_4$:Yb was coated on the surface *via* a seed mediated process. The inert $NaNdF_4$:Yb layer was further coated to form the core-shell-
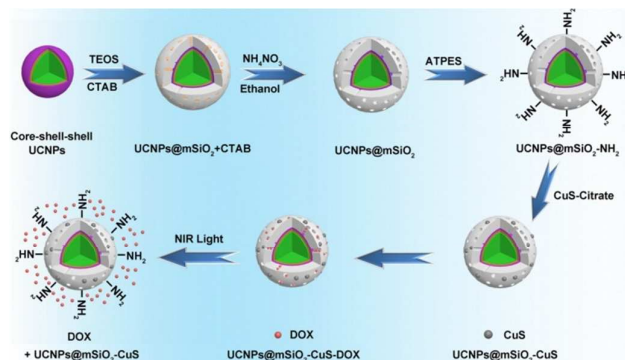
**Scheme 1** Schematic illustration for the synthesis of $NaGdF_4$:Yb,Er@$NaGdF_4$:Yb@$NaNdF_4$@$mSiO_2$-CuS nanoparticles and NIR light triggered DOX release.

shell structured UCNPs. Then the hydrophobic $NaGdF_4$:Yb,Er@ $NaGdF_4$:Yb@$NaNdF_4$:Yb particles dissolved in cyclohexane were transferred into hydrophilic phase using CTAB as the capping agent, which also acted as the surfactant for the subsequent sol-gel reaction to form mesoporous silica layer on $NaGdF_4$:Yb,Er@$NaGdF_4$:Yb@$NaNdF_4$:Yb surface. Finally, the ultra-small CuS nanoparticles are conjugated and well distributed on the surface of UCNPs@$mSiO_2$ through the beneficial electrostatic adsorption. The final product was named as UCMSNs.

The XRD pattern of oleic acid stabilized $NaGdF_4$:Yb,Er@$NaGdF_4$:Yb is shown in Fig. S1A. All the diffraction peaks can be indexed to hexagonal-phased NaGdF4 (JCPDS No. 27–0699). In the XRD of $NaGdF_4$:Yb,Er@$NaGdF_4$:Yb @$NaNdF_4$:Yb (Fig. S1B), the diffractions can be readily indexed to hexagonal $NaNdF_4$ (JCPDS No. 35–1367). However, it is difficult to discern the diffraction and territory of the $NaNdF_4$ shell only from the XRD patterns due to the excellent lattice match between the core and shell materials. In Fig. S1C for the silica coated sample, except for the diffractions ascribed to the hexagonal-phased fluorides, a broad shoulder assigned to amorphous SiO_2 is found at about 22°.
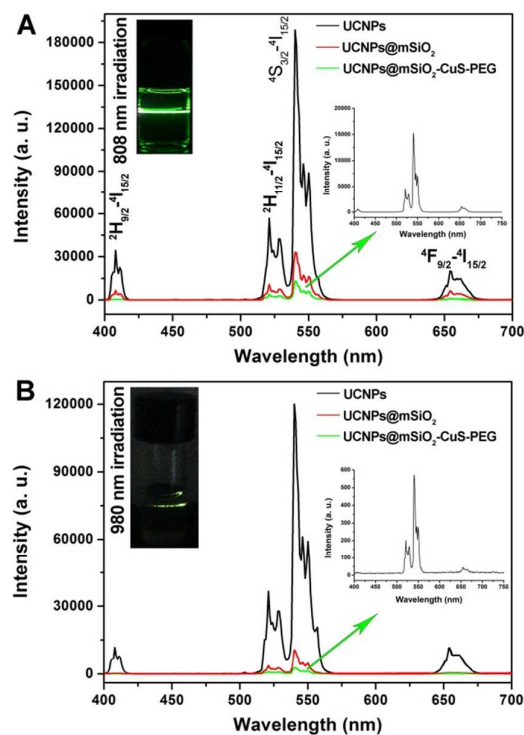
The morphologies, sizes and structures of the products obtained at different synthetic steps are investigated by TEM. In Fig. 1A, the as-prepared $NaGdF_4$:Yb,Er core consists of monodispersed and uniform nanoparticles with a mean diameter of 24 nm. After coating a layer of $NaGdF_4$:Yb, although the core–shell structure cannot be distinguished because of the remarkably similar chemical composition, crystalline phase and electron penetrability between the cores and shells, the average size of the core-shell structure is increased to 27 nm (Fig. 1B), and the high uniformity and dispersibility are well kept. The mean size is further enhanced to 30 nm for the core-shell-shell UCNPs (Fig. 1C). Close observation reveals the obvious core-shell structure with a thin $NaNdF_4$ shell (3 nm) on the inner cores. The TEM image (Fig. 1D) indicates that UCNPs@$mSiO_2$ is composed of well dispersed nanoparticles with the mean diameter of 70 nm. Besides, uniform mesoporous silica layer with worm-like channels can clearly be observed. From Fig. 1E for UCNPs@$mSiO_2$-CuS, we can see that CuS nanoparticles with
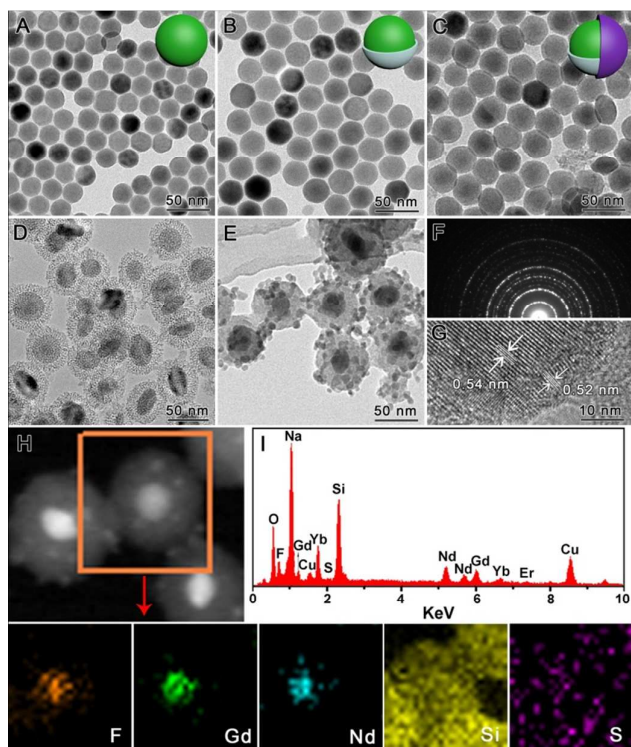
Fig. 1 TEM images of (A) NaGdF$_4$:Yb,Er, (B) NaGdF$_4$:Yb,Er@NaGdF$_4$:Yb, (C) NaGdF$_4$:Yb,Er@NaGdF$_4$:Yb@NaNdF$_4$:Yb, (D) UCNPs@mSiO$_2$, and (E) UCNPs@mSiO$_2$-CuS; (F) SAED, (G) HRTEM image, (H) elemental mapping images, and (I) EDS of UCMSNs.


Fig. 2 UC emission spectra of UCNPs, UCNPs@mSiO$_2$, UCNPs@mSiO$_2$-CuS excited by (A) 808 nm and (B) 980 nm NIR light. Insets are the corresponding digital photographs of the solutions irradiated by NIR laser and the enlarged emission spectra of UCMSNs.

small diameter of 6 nm are firmly attached and well distributed on the surface of UCNPs@mSiO$_2$, forming a typical core-satellite structure due to the electrostatic interaction. The selected area electron diffraction (SAED) image implies the poly-crystalline nature of the sample (Fig. 1F). In the HRTEM image (Fig. 1G), clear fringes with the interplaner spacing of 0.52-0.54 nm can be attribute to the (100) planes of hexagonal NaGdF$_4$ or NaNdF$_4$, demonstrating the high crystallinity of the products. Note that the NaNdF$_4$ shell plays an important role in the UC luminescence when excited by 808 nm laser, which served as sensitizer to harvest 808 nm photons. As given in Fig. S2, the CuS nanoparticles show a good dispersity with an average diameter of 10 nm. In Fig. 1G, the energy dispersive spectroscopy (EDS) of UCNP@mSiO$_2$-CuS confirms the existence of F, Gd, Nd, Si and S elementals, which uniformly distribute evidenced by the elemental mapping image (Fig. 1I).

The N$_2$ adsorption/desorption isotherm (Fig. S3) of UCMSNs can be classified as a type-IV isotherm, indicating the mesoporous channels. The BET surface area and total pore volume are determined to be 536 m^2 g^{-1} and 0.99 cm^3 g^{-1}, and the average pore size is calculated to be 3.1 nm, as shown in the pore size distribution curve (inset, Fig. S3). The high specific surface area and mesoporous pore size make it suitable as carrier for loading anti-cancer drug. Fig. S4A presents the FT-IR spectra of UCNPs, UCNPs@mSiO$_2$-NH$_2$, and UCNPs@mSiO$_2$-CuS, respectively. In the FT-IR spectrum of UCNPs (black line of Fig. S4A), the well-resolved vibrational

peak at 3485 cm^{-1} is assigned to the O-H (COOH) bending vibration. The vibrational peaks at 2916 cm^{-1} and 2854 cm^{-1} are attributed to the –CH$_3$ and –CH$_2$ groups. The peak at 1703 cm^{-1} corresponds to the C=O stretching vibration, and the sharp peaks at 1558 and 1461 cm^{-1} can be ascribed to the –C-O-C– vibrations of the deprotonated carboxylic group (CO$_2^-$). All the peaks are derived from the coated OA molecules.[66] After coating a SiO$_2$ shell and further modification of –NH$_2$ groups, the peaks at 2916 and 2854 cm^{-1} have been markedly weakened, a new band at 1071 cm^{-1} assigned to the Si–O–Si bond and a peak related with –NH$_2$ group at 1639 cm^{-1} appear (red line of Fig. S4A).[67] The variation of the functional groups in FT-IR spectra is also indicative of the successful coating of silica and modification of -NH$_2$. The modification of -NH$_2$ on the surface of UCNPs@mSiO$_2$ has two essential functions: one is to react with biological molecules FA who contains –COOH groups, the other is to induce firm attachment of CuS nanoparticles to the surface of UCNPs@mSiO$_2$ (blue line of Fig. S4A).The UV absorbance intensity of UCMSNs below of 800 nm increases markedly compared with the UV absorbance of UCNPs@SiO$_2$-NH$_2$ NCs (Fig. S4B) indicating that high absorbance of CuS nanocrystals at 808 nm.

It is well known that the Yb^{3+}/Er^{3+} doped rare-earth fluorides emit strong green emission under conventional 980 nm laser excitation. In the emission spectrum of NaGdF$_4$:Yb,Er core (Fig. S5A), the characteristic bands at 521, 540 and 655 nm are ascribed to the $^2H_{11/2} \rightarrow {}^4I_{15/2}$, $^4S_{3/2} \rightarrow {}^4I_{15/2}$, and $^4F_{9/2} \rightarrow {}^4I_{15/2}$ transitions of Er^{3+}, respectively.[68–71] After coating a

NaGdF$_4$:Yb shell (3 nm), the emission intensity of the core-shell structured NaGdF$_4$:Yb,Er@NaGdF$_4$:Yb has been increased by eight times compared with NaGdF$_4$:Yb,Er core. However, the UC emission intensity of the core-shell-shell structure is decreased due to the quenching interaction derived from the introduced Nd^{3+} in the outer shell. As mentioned above, to avoid the overheating and the low penetration depth induced by the conventional 980 nm NIR laser, it is essential to optimize the excitation wavelength to a proper range for biomedical application. The low-cost and high-performance 808 nm NIR laser is thus a selection. In addition, the Nd^{3+} ions have been proved efficient sensitizers to realize high UC emission upon 808 nm excitation. We therefore measured the emission spectra of the core-shell-shell NaGdF$_4$:Yb,Er@NaGdF$_4$:Yb@NaNdF$_4$:Yb UCNPs excited by 808 nm light, which are shown in Fig. 2A. It is obvious that the emission spectrum upon 808 nm excitation is similar to that upon conventional 980 nm excitation except for an increased emission intensity due to the outer NaNdF$_4$:Yb layer. After coating a layer of mesoporous silica, the intensity is clearly decreased owing to the quenching effect by the defects in the mesoporous channels. The emission intensity is further decreased when conjugating CuS NPs with dark-green color. However, the emission intensity is still high enough for biological application, which exhibits bright green emission upon 808 nm irradiation (inset, Fig. 2A). In this core-shell-shell structure, the middle transition layer can efficiently block the non-radiative resonant energy transfer from Er^{3+} ions in the inner core to Nd^{3+} ions in the outer shell by enhancing the interionic distance between two ions, and thus markedly enhance the emission intensity upon the 808 nm excitation (Fig. S5B). As expected, when excited by 980 nm laser, the emission intensities of silica coated and further CuS NPs attached UCNPs are much lower than those upon 808 nm excitation (Fig. 2B). Compared with 980 nm NIR laser, the use of 808 nm NIR laser as the excitation source overcome the overheating issues as well as significantly improve the penetration depth for deep-tissue imaging as shown in fig. S7.

Cell viability, drug release and *in vitro* tumor inhibition ability of UCMSNs. The measurement of biocompatibility of the as-prepared material is necessary for biological application. Fig. 3A shows the HeLa cells after incubation with UCMSNs with different concentration measured by MTT assay. It is found that the sample show high viability of 90-110% in the whole concentration range even high as 500 μg mL^{-1}, while for some other works, the viability only about 80% is reached when cells incubated with 500 μg mL^{-1} samples for the same time,[40,72] indicating the high short-term biocompatibility of the our sample. The high viability over 100% is normal because the cells multiply at an abnormally rapid rate. In order to further certificate the *in vitro* biocompatibility, the hemolytic assay of human red blood cells was performed using deionized water and PBS as positive and negative control, respectively. As shown in Fig. 3B, the red solution in the tubes (inset, Fig. 3B) is caused by the released hemoglobin. No apparently red color is detected in full concentration range, suggesting the negligible hemolysis. It is indicative of the excellent blood compatibility
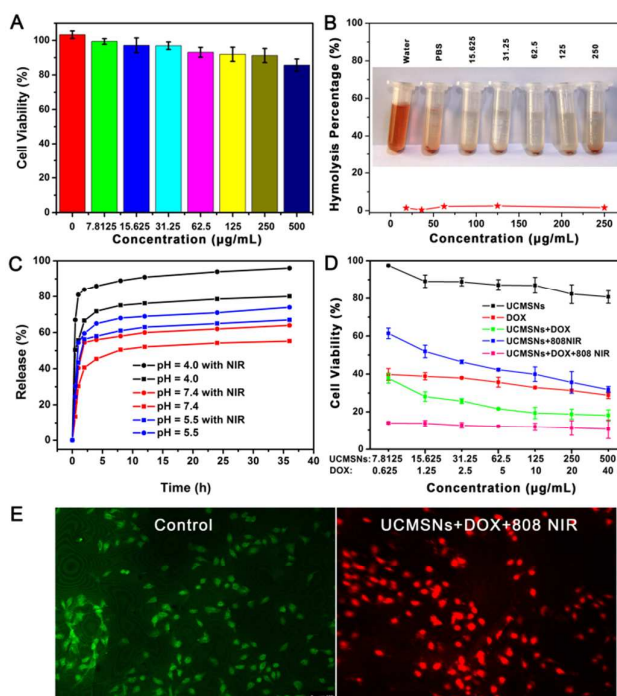

Fig. 3 (A) The viability of HeLa cells incubated with UCMSNs with different concentration for 24 h measured by MTT assay. (B) Hemolytic percentage of human red blood cells incubated with UCMSNs at various concentrations. (C) DOX release efficiency of UCMSNs+DOX at different pH values with and without 808 nm NIR irradiation. (D) *In vitro* HeLa cell viabilities incubated with DOX, UCMSNs, UCMSNs+DOX at various concentrations with and without 808 nm laser NIR. (E) CLSM image of HeLa cancer cells after incubation of culture with laser irradiation and UCMSNs with laser irradiation respectively dyed with calcium AM and PI.

of UCMSNs. Therefore, it can act as a promising platform for anti-cancer treatment due to the high *in vitro* and blood biocompatibility.

DOX was selected as modal anti-cancer drug to study the loading capability and release behavior of the UCMSNs+DOX system. After moderately stirring for 24 h, the DOX loading efficiency is measured to be 65% and the drug loading content is 12%, as determined by UV-vis spectra. In general, the pH value in blood plasma is nearly neutral, while the pH value of cancer cells is weakly acidic due to too much metabolite caused by the fast breeding of cancer cells. Here, pH values of 4.0，5.5 and 7.4 were chosen to detect the pH-dependent release behavior. In Fig. 3C, the cumulative drug release at pH value of 7.4 quickly reaches the equilibrium within 8 h, indicating little DOX is released. By contrast, a much faster release rate has been achieved in acidic surrounding (pH = 4.0). While the release efficiency for pH value of 5.5 is between pH value of 4.0 and 7.4. The enhanced positive charge of UCMSNs under low pH value weakens the electrostatic interaction with positively charged DOX, leading to a faster release. This trend is also ascribed to the increased hydrophilicity and higher solubility of DOX at lower pH caused by increased protonated –NH$_2$ groups on DOX. The result clearly shows the pH-dependent property of the UCMSNs+DOX

Nanoscale Accepted Manuscript

system. In the case of laser irradiation treatment, the UCMSNs+DOX system was irradiation by 808 nm NIR laser for 5 min every hour. The release profiles indicate that the photothermal effect derived from attached CuS nanoparticles under NIR irradiation can effectively promote the DOX release from the systems under all pH conditions.

In the MTT cytotoxicity test, HeLa cells were firstly plated out in 96-well plates at a density of 7000 cells per well and grew for 24 h to allow the cells to attach on the wall of the wells. Then pure UCMSNs, DOX, and UCMSNs+DOX were added to the media, and the cells were incubated at 37 °C for 24 h in 5% CO_2. In Fig. 3D, when pure UCMSNs is added, more than 88% cells are viable in a varying concentration range, indicating that the sample has no obvious toxicity to tumor cells. For the cells incubated with UCMSNs under 808 nm NIR laser irradiation, much lower viability has been obtained due to the thermal effect. When HeLa cells were incubated with pure DOX, the viability is 24.9-39.3% in the concentration range of 7.8125-500 μg mL^{-1}. The viability of the HeLa cells incubated with UCMSNs+DOX in the same concentration range is 18.1-35.7%, which is lower than that of the cells incubated with pure DOX due to the different manner of the drug to enter the cells. It should be noted that the HeLa cells incubated with UCMSNs+DOX with concentrations from 15.63 to 500 μg mL^{-1} with 808 nm NIR irradiation shows the lowest viability (11.3-18.5%), which may be attributed to a synergistic effect from the phtotothermal therapy and the enhanced chemo-therapy induced by a single 808 nm light. The MTT cytotoxicity test on Hepal-6 cells was shown in Figure S8 which is similar with the test on HeLa cells. And the Hepal-6 cells
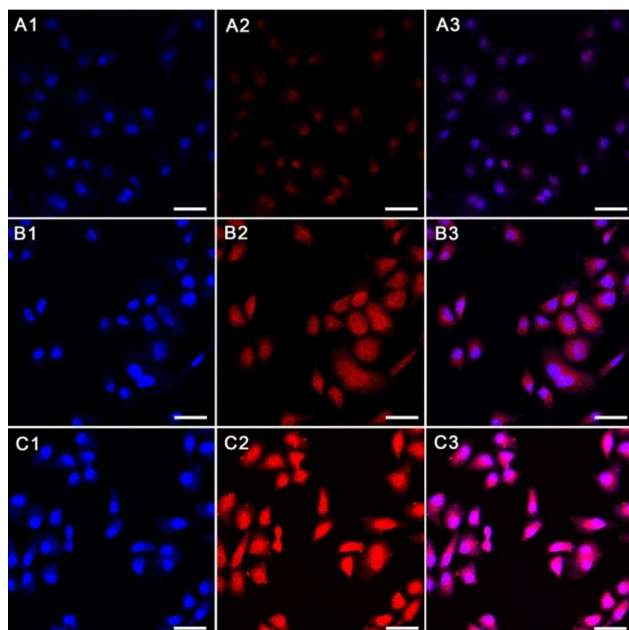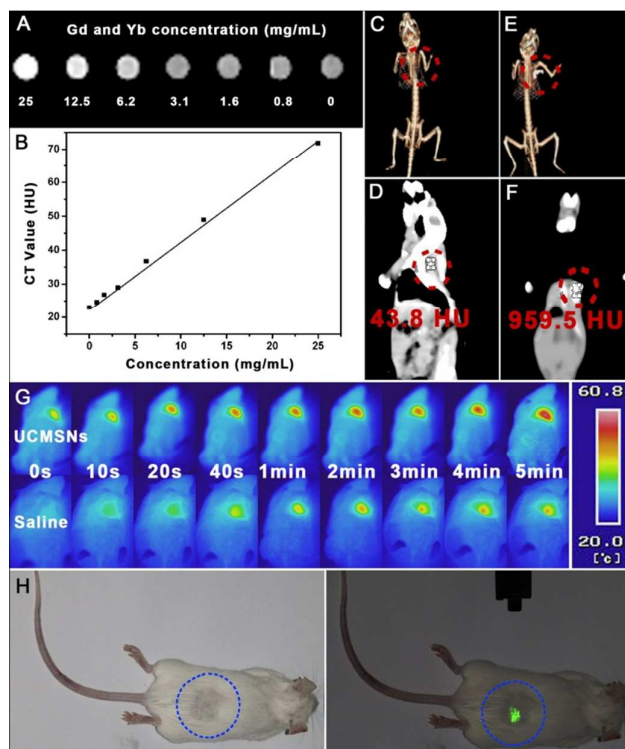
Fig. 5 (A) *In vitro* CT images of UCMSNs *versus* Gd and Yb concentrations. (B) CT value of aqueous UCMSNs solution as a function of the particle concentration. CT images of tumor-bearing Balb/c mice (C, D) before and (E, F) after intratumoral injection. (G) Infrared thermal images of tumor-bearing mice after intratumoral injection of UCMSNs and saline *versus* irradiation time. (H) Subcutaneous implantation test of UCMSNs on a mouse irradiated by 808 nm light.

incubated with UCMSNs + DOX with the concentrations from 15.63 to 500μg mL^{-1} with 808 nm NIR irradiation also shows the lowest viability (10.45-19.0%), which may also because of a synergistic effect from the photothermal therapy and the enhanced chemo-therapy induced by a single 808 nm light.

Calcein AM which could mark living cells with green color and PI which could mark died cells with red color were used to dye HeLa cells under different conditions detected by CLSM to prove the killing effect. In the CLSM images of HeLa cells in culture irradiated with 808 nm NIR laser (left, Fig. 3E), almost all of the cells are green which indicates the pure culture has no absorbance of NIR irradiation. However, when HeLa cells were incubated with UCMSNs+DOX and irradiated by 808 nm NIR laser for 5 min, almost only red cells can be found (right, Fig. 3E), indicating the tumor cells are effectively killed due to the synergistic chemo- and photothermal effect.

To further verify the location of UCMSNs+DOX relative to the cells, the CLSM images of HeLa cells incubated with the composite for 0.5, 1, and 3 h at 37 °C are given in Fig. 4. The red fluorescence of DOX can be clearly seen in confocal images when excited with a wavelength of 488 nm. When the UCMSNs which loading DOX were uptake by cells, the DOX will be released because of the PH value of the cells is about 7. After 30 min, the red DOX appears localized as scattered dots,

Fig. 4 CLSM image of HeLa cells incubated with UCMSNs+DOX for (A1-A3) 30 min, (B1-B3) 1 h and (C1-C3) 3 h at 37 °C. Each series can be classified to the nuclei of cells (dyed in blue by DAPI for visualization), UCMSNs+DOX, and a merge of the two above channels. The scale bar in each image is 50 μm.
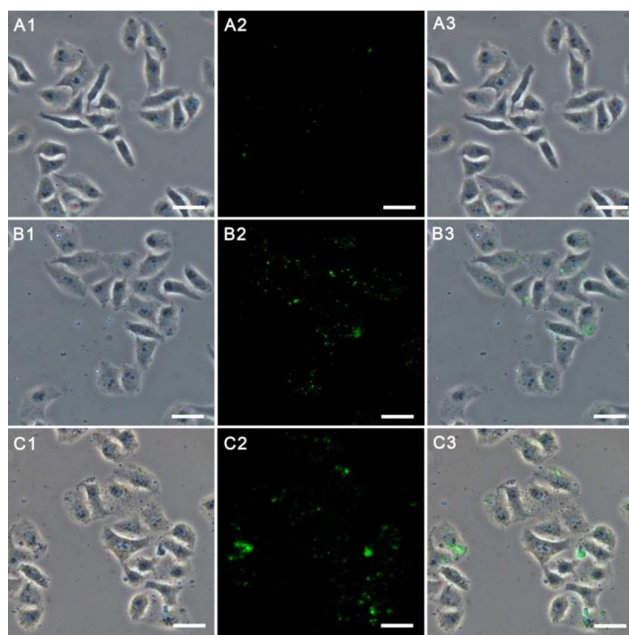
Fig. 6 Inverted fluorescence microscope images of HeLa cells incubated with UCMSNs for (A1-A3) 30 min, (B1-B3) 1 h and (C1-C3) 3 h at 37 °C. Each series can be classified to the bright field image, UC luminescence image and overlay of two above. The scale bar in each image is 50 μm.

Fig. 7 (A) *In vivo* tumor volume changes of Balb/c mice in different groups under various treatments as a function of the treated time. The relative tumor volumes are normalized to their initial volumes before the treatment. (B) Photographs of excised tumors from representative Balb/c mice after 14 day treatment. (C) Body weight changes of Balb/c mice under various treatments *versus* time. Error bars indicate the standard deviations. (D) The corresponding digital photos of mice after treatments. (E) H&E stained images of tumor sections after 14 day treatment from different groups.

which indicates that only a few of the particles have been taken up by HeLa cells. With the prolonged incubation time, the intensities of red signal increases, which may means more nanoparticles cross the membrane and are localized in the nucleus. The results confirm that the as-prepared sample can be effectively taken up by HeLa cells.

CT/MRI/UCL multimodal imaging properties. X-ray CT has been proved an effective diagnostic imaging technique owing to the deep tissue penetration and high resolution. Because Yb^{3+} and Gd^{3+} doped crystals can be employed as contrast agents for CT imaging, we therefore measured the CT contrast efficacy of as-synthesized UCMSNs. As shown in Fig. 5A,B, the CT values and signal intensity increase with the concentration of the sample. *In vivo* CT imaging was further investigated by intratumorally injecting UCMSNs into tumor-bearing mice (Fig. 5C-F). As shown, the CT value in the tumor is up to 959.5 HU (Hounsfield Units) compared with the control of 43.8 HU (without injection) from the transversal position. The results reveal the as-prepared UCMSNs can be used as CT imaging agent. Fig. S6A gives the *In vitro* T1-weighted MR images of UCMSNs *versus* the Gd concentration. We can see that the signals positively increase with the Gd concentration from 0 to 5 mM. The longitudinal relaxivity (R_1) value of the sample is determined to be 2.239 mM^{-1} s^{-1} (Fig. S6B). Fig. 5G shows the *in vivo* infrared thermal images of tumor-bearing mice after injection of UCMSNs and saline as a function of the exposure time under the 808 nm laser irradiation. It is apparent that the group injected with UCMSNs has obviously higher temperature (up to 52.8 °C) than that (41.8 °C) injected with saline, which should be caused by the thermal effect induced by NIR light. Therefore, the combination of nanomaterials-chemotherapy with photo thermal ablation will offset the disadvantage of on

chemotherapy alone on the deep-seated tumor. More importantly, the photo thermal ablation will promote drug release as shown in Fig. 3 C, indicating that the chemo-therapy and photo-thermal could effectively combine mutual advantages together generate a strong synergistic effect, and then leading to a much better antitumor efficacy than the two treatment alone or even the projected sum of the two treatments.

For UCL imaging assay, the HeLa cells show evident green luminescence irradiated by 808 nm laser after incubated with UCMSNs at 37 °C for 30 min, 1 h and 3 h (Fig. 6). Meanwhile, the gradually enhanced green emission implies more and more particles are internalized into the cells with the increased incubation time. The result indicates that UCMSNs can be used as luminescence probe for cell imaging and monitoring the cell endocytosis process. To investigate the *in vivo* UCL imaging of as-synthesized UCMSNs, a mouse after hypodermic injection of UCMSNs to the subcutaneous tissue of back (the marked area) and another mouse injected with saline as a control under 808 nm irradiation are presented in Fig. 5H. Obviously, the mouse injected with UCMSNs exhibits bright green color, while the region of the mouse injected with saline shows original color.

In Vivo synergistic therapy. To further evaluate the *in vivo* tumor inhibition efficacy of UCMSNs+DOX under 808 nm laser irradiation, here we selected liver cancer tumor line H22 (murine hepatocarcinoma) as the xenograft model. The tumor-bearing Balb/c mice were randomized into six groups (n = 5, each group) and were treated by intratumoral injection with pure UCMSNs with and without 808 nm NIR irradiation, DOX,

Nanoscale Accepted Manuscript

ARTICLE
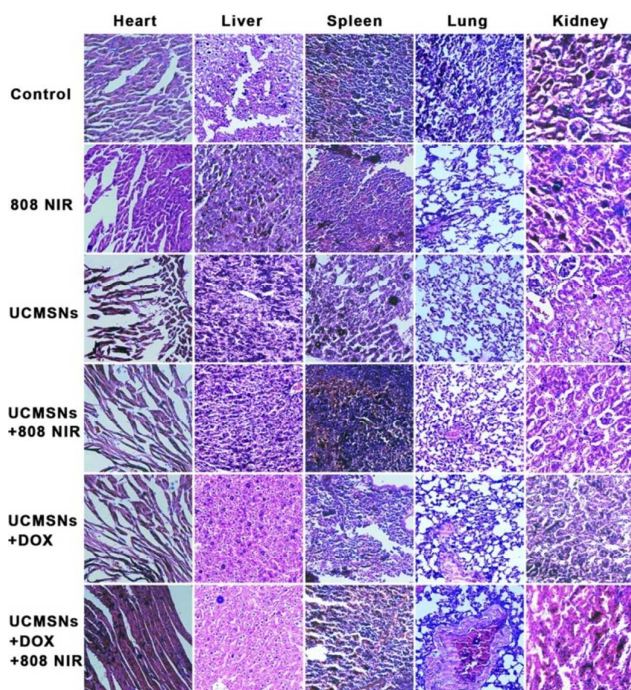
Fig. 8 H&E stained images of heart, liver, spleen, lung, and kidney collected from different groups.

and UCMSNs+DOX with and without NIR irradiation, respectively. The group which was injected with nonthing was used for blank control. 100 μL (1 mg mL^{-1}) of solution was injected every two days, and the amount of pure DOX is consistent with that of UCMSNs+DOX. After various treatments, the result of each group is much different (Fig. 7A). The tumor size is large without any injection, while the tumors of the mice treated under other condition are inhibited to different extent. It is noted that when the NIR irradiation is utilized, clear inhibition occurs due to the photothermal and/or enhanced chemo-therapies. The difference between group 5 and group 6 indicates that a combined photothermal and chemo-therapy should play the key role in the therapy efficacy. It is obvious that the group treated with UCMSNs+DOX under 808 NIR irradiation shows the best tumor growth inhibition efficacy, which is proved by the digital photographs of mice excised tumors (Fig. 7B). In addition, the body weight is an important parameter to assess the systemic toxicity of the material to the body. In Fig. 7C, the body weight of the mice in all groups doesn't decrease with the prolonged time, implying the little adverse side-effect of UCMSNs+DOX compared with traditional anti-cancer drugs. The digital photographs of representative mice with tumors (Fig. 7D) also directly show that the tumor size of the mouse in group 6 has markedly been decreased compared with that in control group. Fig. 7E shows the tumor histologic sections of the groups treated with different conditions. It is found that the shape, size, and staining of the tumor cells in the control group are at variance, and most of the nucleus have the mitotic phenomena. For the best inhibition group (group 6), owing to the markedly increased apoptotic and necrotic tumor cells,

the cells in this groups seems almost regular with normal cells.

The representative H&E stained images of the heart, liver, spleen, lung and kidney organs from the mice in different groups are displayed in Fig. 8. Histology analysis of the major organs from mice after injection of UCMSNs+DOX with 808 nm NIR light irradiation indicates that no appreciable abnormality or noticeable organ damage can be found, and the intercellular gap is ambiguous in the liver organ and there are remarkably atrophy in the glomerulus. All the results preliminarily prove that the UCMSNs+DOX under 808 NIR light mediated PTT could be a safe and practical cancer treatment technique with substantial clinical potential.

Conclusions

In summary, a multifunctional nanotheranostic for multimodal imaging and cancer ablation by chemo-/ photothermal synergistic therapy has been constructed. The *in vitro* and *in vivo* result indicated these UCMSNs can not only convert 808 nm NIR laser into heat for effective eradication of cancer cells, but induce an obviously enhanced DOX release, which results in a synergistic therapeutic effect. Besides the CT and MRI imaging properties, the nanocomposite also exhibit good UCL and PTT imaging effects *in vivo* when excited by a single 808 nm NIR laser. We believe that this multifunctional hybrid system should be a promising platform to achieve imaging-guided therapy.

Experimental section

Materials and Synthesis. All the chemical reagents used in this experiment are of analytical grade without any further purification. Gd_2O_3 (99.99%), Yb_2O_3 (99.99%), Er_2O_3 (99.99%) and Nd_2O_3 (99.99%) were all purchased from Sinopharm Chemical Reagent Co., Ltd. (China). Oleic acid (OA), 1-octadecene (ODE), 1-(3-dimethylaminopropyl)-3-ethyl carbodiimide hydrochloride (EDC), N-hydroxysuccinimide (NHS), folic acid (FA), and 3-[4,5-dimethylthiazol-2-yl]-2,5-diphenyl tetrazolium bromide (MTT) were purchased from Sigma-Aldrich Co. LLC (China). Doxorubicin (DOX) was purchased from Nanjing Duodian Chemical Limited Company. Hydrochloric acid (HCl), sodium oleate ($C_{18}H_{33}NaO_2$), hexane, sodium fluoride (NaF), tetraethylorthosilicate (TEOS), cetyltrimethylammonium bromide (CTAB, ≥99%), sodium citrate ($Na_3C_6H_5O_7$), sodium sulphide (Na_2S), trifluoroacetic acid (CF_3COOH), sodium trifluoroacetate (CF_3COONa) were purchased from Beijing Chemical Corporation (China).

Synthesis of OA-stabilized β-NaGdF$_4$:Yb,Er. OA-capped β-NaGdF$_4$:Yb,Er nanoparticles were synthesized according to a modified procedure.[66] In a typical process, 1 mmol of RE(oleate)$_3$ (RE = 80%Gd + 18%Yb + 2%Er), 12 mmol of NaF, and 20 mL of OA/ODE (v/v = 1:1) mixed solvent were added to the reaction vessel and heated to 110 °C under a vacuum for 30 min to remove residual water and oxygen. After that, the temperature was increased to 300 °C and kept for 1.5 h in N_2 atmosphere. β-NaGdF$_4$:Yb,Er nanoparticles were then

obtained by washing the sample with acetone and cyclohexane several times.

Synthesis of OA-stabilized core-shell structured NaGdF$_4$:Yb,Er@NaGdF$_4$:Yb. Briefly, 1 mmol CF$_3$COONa, 0.9 mmol Gd(CF$_3$COO)$_3$, 0.1 mmol Yb(CF$_3$COO)$_3$ and as-prepared β-NaGdF$_4$:Yb,Er NPs were added to a mixture of 20 mL OA and 20 mL ODE in a three-necked flask at room temperature. The solution was pre-degassed for 30 min under vigorous stirring then heated to 120 °C under vacuum for 30 min to remove water and oxygen, and a transparent solution was thus formed. After that, the solution was heated to 305 °C and kept for 0.5 h in Ar. After naturally cooling to room temperature, an excess amount of ethanol was added into the solution. The mixture was centrifugated at 5000 pm for 5 min, washed with ethanol and cyclohexane several times. The resultant NPs was re-dispersed in cyclohexane.

Synthesis of OA-stabilized core-shell-shell structured NaGdF$_4$:Yb,Er@NaGdF$_4$:Yb@NaNdF$_4$:Yb. The synthetic procedure of NaGdF$_4$:Yb,Er@NaGdF$_4$:Yb@NaNdF$_4$:Yb was similar to that of NaGdF$_4$:Yb,Er@NaYF$_4$:Yb nanocrystals, except that 1 mmol CF$_3$COONa, 1 mmol RE(CF$_3$COO)$_3$ (RE = 90%Nd + 10%Yb) and as-synthesized NaGdF$_4$:Yb,Er@NaYF$_4$:Yb nanoparticles were added to a mixture of OA (20 mL) and ODE (20 mL) in a three-necked flask and maintained at 305 °C for 30 min. The final core-shell-shell structured NaGdF$_4$:Yb,Er@ NaGdF$_4$:Yb@NaNdF$_4$:Yb up-conversion nanoparticles was denoted as UCNPs, which was re-dispersed in cyclohexane.

Synthesis of UCNPs@mSiO$_2$. UCNPs@mSiO$_2$ nanoparticles were synthesized according to the modified procedure we reported.[67] Typically, 2 mL cyclohexane solution containing UCNPs (about 5-10 mg mL^{-1}) was mixed with 0.1 g CTAB and 20 mL water. The mixture was then stirred vigorously to evaporate cyclohexane at room temperature, leading to a transparent UCNPs-CTAB solution. For coating mesoporous silica shells onto UCNPs, 10 mL of the aqueous CTAB stabilized UCNPs solution was added to the mixture of 20 mL water, 3 mL ethanol and 150 μL NaOH solution (2 M). The mixture was heated to 70 °C under stirring. Then 160 μL of TEOS was added into the solution and stirred for 10 min. The as-obtained product was centrifuged and washed with ethanol several times. The CTAB was removed *via* an exchanged method, where the as-synthesized UCNPs@mSiO$_2$ (20 mg) was transferred to 50 mL ethanol containing 0.3 g NH$_4$NO$_3$ and heated at 60 °C for 2 h. Finally, the UCNPs@mSiO$_2$ NPs with mesoporous silica shell were obtained and dispersed in ethanol.

Synthesis of UCNPs@mSiO$_2$-FA. In a brief procedure, 50 mg of UCNPs@mSiO$_2$ nanoparticles were dispersed in 30 mL of ethanol. 125 μL of deionized water and 125 μL of APTES were added and heated to 45 °C for 8 h under stirring. The UCNPs@mSiO$_2$-NH$_2$ nanoparticles were obtained by centrifugation, washed with ethanol several times. FA molecules were conjugated to the UCNPs@mSiO$_2$ surface by coupling NHS and EDC. Briefly, 1 mg of FA, 2 mg of NHS and 6 mg of EDC were dissolved into 20 mL of deionized water and stirred in dark for 2 h. After that, 20 mg of UCNPs@mSiO$_2$-NH$_2$ was added and stirred for one night in dark. The sample was

collected by centrifugation and washed with deionized water and ethanol to remove free FA molecules.

Synthesis of CuS nanoparticles. Typically, 34.1 mg of CuCl$_2$ and 40 mg of sodium citrate were dissolved in 180 mL deionized water, then 20 mL sodium sulfide solution (2 mg/mL) was added under stirring. After stirred for 5 min at room temperature, the mixture was heated to 90 °C and kept for 15 min, and then transferred to ice-cold water. At last, a dark-brown solution containing citrate-coated CuS nanoparticles was prepared and then stored at 4 °C for further use.

Synthesis of UCNPs@mSiO$_2$-FA-CuS-PEG nanoparticles. UCNPs@mSiO$_2$-FA-CuS-PEG nanoparticles were synthesized by electrostatic adsorption. Briefly, 10 mg of UCNPs@mSiO$_2$-FA nanoparticles were added into above 30 mL CuS solution and dispersed by ultrasonication. After stirred for 1 h, the product was recovered by centrifugation and washed with deionized water two times. The as-prepared UCNPs@mSiO$_2$-FA-CuS nanoparticles were prepared and dispersed in 20 mL deionized water. Then, 10 mg PEG-NH$_2$ was added into the solution and stirred for another 24 h for attaching PEG molecules. UCNPs@mSiO$_2$-FA-CuS-PEG was obtained by centrifugation and washed with deionized water three times. The final UCNPs@mSiO$_2$-FA-CuS-PEG up-conversion mesoporous silica nanoparticles were denoted as UCMSNs.

Characterization. Powder X-ray diffraction (XRD) patterns were measured on a Rigaku D/max TTR-III diffractometer at a scanning rate of 5°/min in 2θ range from 20 to 80° using Cu-Kα radiation (λ = 0.15405 nm). Transmission electron microscopy (TEM) high-resolution transmission electron microscopy (HRTEM) images were obtained on a FEI Tecnai G^2 S-Twin instrument. Up-conversion emission spectra were acquired on Edinburgh FLS980 apparatus using 980 nm and 808 nm LD Module as the excitation source and detected from 400–700 nm. N$_2$ adsorption/desorption was measured on a Micrometrics Tristar II apparatus. The specific surface area was obtained from the Brunauer-Emmett-Teller (BET) method, and pore size distribution was calculated from the desorption branch of the isotherm. FT-IR spectra were obtained from an AVATAR 360 FT-IR spectrophotometer using a KBr technique. DOX concentration was detected by UV-1601 UV-vis spectrophotometer.

DOX loading and release test. 10 mg UCMSNs were dispersed in 5 mL of PBS (pH = 7.4). Then, 2.5 mg DOX was added into the solution with slow string for 24 h under dark condition. The DOX-loaded sample was collected by centrifugation and then the supernatant solution was kept ultraviolet visible (UV-vis) analysis. After, as-prepared UCMSNs + DOX samples were immersed in 10 mL of phosphoric acidic buffer solutions (PBS) with pH values of 4.0, 5.5and 7.4 at 37 °C with slow stirring. At determined time interval, PBS was taken by centrifugation and replaced with same amount of fresh PBS. Especially, for the DOX release rate under near infrared (NIR), near infrared (NIR) irradiation (808 nm, 2 W cm^{-2}) was used during the whole drug release process. The laser probe with a 15 mm spot diameter was placed on the top of the experimental tube. The concentration of released DOX in the

supernatant solutions was determined at the wavelength of 480 nm by UV-vis measurement. According to the standard curve $A_{480nm} = 0.0187C + 0.0233$, the release amount of DOX from nanoparticles can be calculated. The DOX loading content was calculated as following: IE %$=(M_1 - M_2)/M_1 \times 100\%$ (M_1 is total drug and M_2 is drug in supernatant),and the loading efficiency of DOX, which is 65% was also obtained.

Cell viability of UCMSNs. MTT cell assay performed on the HeLa cells was employed to evaluate the biocompatibility. Typically, HeLa cells were plated out at a density of 6000–7000 cells per well in a 96-well plate and incubated with UCMSNs overnight at 37 °C in a humidified atmosphere containing 5% CO_2 to allow the cells to attach on the wells. The UCMSNs were sterilized by autoclaving, and then a series of concentrations of the nanoparticles were added and incubated at 37 °C for 24 h in 5% CO_2. 5 mg mL^{-1} stock solution of MTT was prepared in PBS and this stock solution (20 µL) was added to each well containing different amount of UCMSNs. The plates were incubated at 37 °C for another 24 h. The medium and MTT were then removed, and the MTT-formazan particles were dissolved in 150 µL DMSO and placed on a shaking table at 150 rpm for 5 minutes.

In vitro **cytotoxicity assay**. *In vitro* cytotoxicity of the samples was assayed against HeLa cancer cells. Typically, HeLa cells were seeded in a 96-well plate with a density of 7000 cells per well and cultured at 37 °C for 24 h in 5% CO_2. HeLa cells were then treated with UCMSNs for about 4 h, then irradiated with 808 nm lasers for 40 min (4.5 W cm^{-2}, 5 min break after 5 min irradiation). As the control, the HeLa cells treated with DOX loaded UCMSNs under 808 nm lasers for 40 min (4.5 W cm^{-2}, 5 min break after 5 min irradiation), and the HeLa cells only treated with UCMSNs were left in the dark. After that, the cells were incubated for another 24 h in the dark. The concentrations of DOX were fixed at 0.625, 1.25, 2.5, 5, 10, 20, and 40 µg mL^{-1}. At the end of the incubation, the cells were then treated with MTT solution (diluted in a culture medium with a final concentration of 5 mg mL^{-1}) and incubated for another 4 h. Subsequently, the supernatant was removed, and 150 µL of DMSO was added to each well before the plate was examined using a microplate reader at the wavelength of 490 nm. And the progress on *in vitro* cytotoxicity of the samples assayed against Hepal-6 cells was similar with the HeLa cells.

Hemolysis Assay. Red blood cells were obtained by removing the serum from the EDTA. K2 stabilized human blood through washing with PBS solution for five times until the supernatant. Then the blood cells were diluted to 1/10 with PBS solution (pH = 7.4). Diluted cells suspension (0.3mL) was then mixed with (1) 1.2 mL of deionized water as a positive control; (2) 1.2 mL of PBS as a negative control; and (3) 1.2 mL of materials suspensions with varying concentration (15.625, 31.25, 62.5, 125, and 250 µg/mL^{-1}). Then the samples were shaken and keep stable for 2 h at room temperature. Finally, the mixture were centrifuged and the absorbance of the upper supernatants was measured by UV-vis. The percentage of hemolysis was calculated using the following equation

$$\text{Hemolysis\%} = （A_{\text{sample}} - A_{\text{control(-)}}）/ (A_{\text{control(+)}} - A_{\text{control(-)}})$$

where A is the absorbance of UV-vis spectrum.

Cellular uptake of UCMSNs. The cellular uptake by HeLa tumor cells was studied by a confocal laser scanning microscope (CLSM, Leica TCS SP8). HeLa cancer cells were firstly cultured in a 6-well plate and grew overnight to get a monolayer. Then, the cells were incubated with UCMSNs+DOX for 0.5 h, 1 h, 3 h, and 6 h at 37 °C, respectively. Then, the cells were washed with PBS solution, fixed for 10 min with 2.5% formaldehyde (1 mL $well^{-1}$), and rinsed with PBS several times. After that, the cells were stained with DAPI solution (1 mL $well^{-1}$, 20 µg mL^{-1} in PBS) for 10 min so as to carry out nucleus labeling. Finally, the dyed cells were washed with PBS several times. The coverslips were fixed on a glass microscope slide, and the fluorescence images were recorded by CLSM instrument (Leica TCS SP8).

UCL microscopy observation of UCMSNs. HeLa cells (105 $well^{-1}$) were seeded in 6-well culture plates and grown overnight as a monolayer and then were incubated with UCMSNs for different times at 37 °C. Subsequently, the cells were washed with PBS three times, fixed with 2.5% formaldehyde (1 mL $well^{-1}$) at 37 °C for 10 min, and washed with PBS three times. The UCL measurement was performed on an inverted fluorescence microscopy (Nikon Ti–S), and an external CW 808 nm laser was introduced to illuminate the samples.

In vitro **and** *In vivo* **X-ray CT imaging**. The *in vitro* CT images were obtained from a Philips 64-slice CT scanner at voltage of 120 kV. Typically, UCMSMs with concentration of 0.8, 1.6, 3.1, 6.2, 12.5 and 25 mg mL^{-1} were first dispersed in PBS and then added in a series of tubes (2 mL) for CT measurement. In order to carry out in vivo CT measurement, the Balb/c mice were firstly anesthetized with 10% chloral hydrate by intra-peritoneal injection. After that, 100 µL of UCMSNs were injected intratumorally into the tumor-bearing mice, which were scanned before and after injection.

In vitro T_1-**weighted MR imaging**. The *in vitro* MRI measurement was carried out on a 0.5 T MRI magnet (Shanghai Niumai Corporation Ration NM120-Analyst). UCMSNs were first dispersed in deionized water with diverse Gd concentrations (determined by ICP-MS). T_1 measurement was performed by a nonlinear fit to changes in the mean signal intensity within each well *versus* repetition time (TR) with a Huantong 1.5 T MR scanner. T_1 was acquired *via* an inversion recovery sequence. At last, the r_1 relaxivity values were calculated by the curve fitting of $1/T_1$ relaxation time (s^{-1}) as a function of the Gd concentration (mM).

In vivo **toxicity of UCMSNs and UCMSNs+DOX**. Female Balb/c (25-35 g) were purchased from Harbin Veterinary Research Institute, Chinese Academy of Agricultural Sciences (Harbin, China), and all the mouse experiments were performed in compliance with the criterions of The National Regulation of China for Care and Use of Laboratory Animals. Firstly, the tumors were established by subcutaneous injection of H22 cells (murine hepatocarcinoma cell lines) in the left axilla of each mouse. After 4 days, each tumor size reaches about 100-200 mm. The tumor-bearing mice were randomly

Nanoscale Accepted Manuscript

separated into six groups and each group has five mice. Then the mice were treated by intratumoral injection with pure UCMSNs, UCMSNs+DOX, UCMSNs+808 NIR, and UCMSNs+DOX+808 NIR. The group was used for control without any injection. The injected amount is 80 µL (1 mg mL^{-1}) and injected every two days, and the pure DOX was consistent with the materials. For the NIR irradiation, we irradiated the tumor site with 808 nm laser (4.5 W cm^{-2}) for 10 min. The body weights and tumor volumes were monitored every day after treatment.

   Histology Examination. Histology analysis was started at the 14th day after treatment. The tumors and organs (heart, liver, spleen, lung, and kidney) of the mice in each group were isolated, fixed with a 4% formaldehyde solution for 24 h at room temperature before embedded with paraffin. After dehydration, the dry weights of heart, liver, spleen, lung, kidney and tumor were recorded. After paraffin embedding, fine 5 µm slices of the organs or tissues were stained with hematoxylin and eosin (H&E) and studied for histological changes examined by a microscope (Leica TCS SP8).

Acknowledgements

Notes and references

1   J. Zhou, Z. Liu, F. Li, *Chem. Soc. Rev.*, 2012, **41**, 1323-1349.
2   Z. Gu, L. Yan, G. Tian, S. Li, Z. Chai, Y. Zhao, *Adv. Mater.*, 2013, **25**, 3758-3779.
3   Y. Dai, P. A. Ma, Z. Cheng, X. Kang, X. Zhang, Z. Hou, C. Li, D. Yang, X. Zhai, J. Lin, *ACS Nano*, 2012, **6**, 3327-3338.
4   Y. Chen, H. Chen, D. Zeng, Y. Tian, F. Chen, J. Feng, J. Shi, *ACS Nano*, 2010, **4**, 6001-6013.
5   S. Gai, P. Yang, C. Li, W. Wang, Y. Dai, N. Niu, J. Lin, *Adv. Funct. Mater.*, 2010, **20**, 1166-1172.
6   M. L. Yin, Z. H. Li, E. G. Ju, Z. Z. Wang, K. Dong, J. S. Ren, X. G. Qu, *Chem. Commun.*, 2014, **50**, 10488-10490.
7   G. K. Such, A. P. R. Johnston, F. Caruso, *Chem. Soc. Rev.*, 2011, **40**, 19-29.
8   G. Le Duc, I. Miladi, C. Alric, P. Mowat, E. Bräuer-Krisch, A. Bouchet, E. Khalil, C. Billotey, M. Janier, F. Lux, T. Epicier, P. Perriat, S. Roux, O. Tillement, *ACS Nano*, 2011, **5**, 9566-9574.
9   M.-Y. Chang, A.-L. Shiau, Y.-H. Chen, C.-J. Chang, H. H. W. Chen, C.-L. Wu, *Cancer Sci.*, 2008, **99**, 1479-1484.
10 Y. Prezado, G. Fois, G. Le Duc, A. Bravin, *Med. Phys.*, 2009, **36**, 3568-3574.
11 K. Kobayashi, N. Usami, E. Porcel, S. Lacombe, C. Le Sech, *Mutat. Res./Rev. in Mutat.*, 2010, **704**, 123-131.
12 Paul, A. Narasirnhan, F. J. Kahlen, S. K. J. Das, *Therm. Biol.*, 2014, **41**, 77-87.
13 J. Kim, J. E. Lee, J. Lee, J. H. Yu, B. C. Kim, K. An, Y. Hwang, C.-H. Shin, J.-G. Park, J. Kim, T. Hyeon, *J. Am. Chem. Soc.*, 2005, **128**, 688-689.
14 Q. Tian, M. Tang,; Y. Sun, R. Zou, Z. Chen, M. Zhu, S. Yang, J. Wang, J. Wang, J. Hu, *Adv. Mater.*, 2011, **23**, 3542-3547.
15 J. Yang, D. Shen, L. Zhou, W. Li, X. Li, C. Yao, R. Wang, A. M. El-Toni, F. Zhang, D. Zhao, *Chem. Mater.*, 2013, **25**, 3030-3037.
16 G. B. Shan, R. Weissleder, S. A. Hilderbrand, *Theranostics* 2013, **3**, 267-274.
17 Z. X. Li, J. C. Barnes, A. Bosoy, J. F. Stoddart, J. I. Zink, *Chem. Soc. Rev.*, 2012, **41**, 2590-2605.
18 X. Ye, D. Reifsnyder Hickey, J. Fei, B. T. Diroll, T. Paik, J. Chen, C. B. Murray, *J. Am. Chem. Soc.*, 2014, **136**, 5106-5115.
19 P. Hillemanns, L. Wolber, J. Juckstock, P. Neuser, F. Hilpert, P. Harter, N.De Gregorio, A. Hasenburg, J. Sehouli, A. Habermann, *Oncologie*. 2014, **37**, 70-70.
20 M. M. Gottesman, T. Fojo, S. E. Bates, *Nat. Rev. Cancer* 2002, **2**, 48-58.
21 N. S. Russell H. Bartelink, *Cancer Treat. Rev.*, 1999, **25**, 365-376.
22 S. L. Gai, C. X. Li, P. P. Yang, J. Lin, *Chem. Rev.* 2014, **114**, 2343–2389.
23 Z. Li, Y. Zhang, S. Jiang, *Adv. Mater.*, 2008, **20**, 4765-4769.
24 J. Yang, Y. Deng, Q. Wu, J. Zhou, H. Bao, Q. Li, F. Zhang, F. Li, B. Tu, D. Zhao, *Langmuir*, 2010, **26**, 8850-8856.
25 Z. Liu, L. Sun, F. Li, Q. Liu, L. Shi, D. Zhang, S. Yuan, T. Liu, Y. Qiu, *J. Mate. Chem.*, 2011, **21**, 17615-17618.
26 F. Zhang, G. B. Braun, A. Pallaoro, Y. Zhang, Y. Shi, D. Cui, M. Moskovits, D. Zhao, G. D. Stucky, *Nano Lett.*, 2011, **12**, 61-67.
27 F. Wang, X. Liu, *Chem. Soc. Rev.*, 2009, **38**, 976-989.
28 D. Tu, L. Liu, Q. Ju, Y. Liu, H. Zhu, R. Li, X. Chen, Angew. Chem. Int. Ed., 2011, **50**, 6306-6310.
29 J. Wang, F. Wang, C. Wang, Z. Liu, X. Liu, *Angew. Chem. Int. Ed.*, 2011, **50**, 10369-10372.
30 J. Kim, Y. Piao, T. Hyeon, *Chem. Soc. Rev.*, 2009, **38**, 372-390.
31 Q. Zhang, B. Yan, *Chem. Commun.*, 2011, **47**, 5867-5869.
32 M. Haase, H. Schäfer, *Angew. Chem. Int. Edit.*, 2011, **50**, 5808-5829.
33 L. D. Carlos, R. A. S. Ferreira, V. D. Z. Bermudez, B. Julian-Lopez, P. Escribano, *Chem. Soc. Rev.*, 2011, **40**, 536-549.
34 J. Zhuang, J. Wang, X. Yang, I. D. Williams, W. Zhang, Q. Zhang, Z. Feng, Z. Yang, C. Liang, M. Wu, Q. Su, *Chem. Mater.*, 2009, **21**, 160-168.
35 S.-S. Wang, W.-T. Chen, Y. Li, J. Wang, H.-S. Sheu, R.-S. Liu, *J. Am. Chem. Soc.*, 2013, **135**, 12504-12507.
36 K. A. Abel, J.-C. Boyer, F. C. J. M. van Veggel, *J. Am. Chem. Soc.*, 2009, **131**, 14644-14645.
37 J. Hao, Y. Zhang, X. Wei, *Angew. Chem. Int. Ed.*, 2011, **50**, 6876-6880.
38 Q. Ju, D. Tu, Y. Liu, R. Li, H. Zhu, J. Chen, Z. Chen, M. Huang, X. Chen, *J. Am. Chem. Soc.*, 2012, **134**, 1323-1330.
39 F. Chen, W. Bu, S. Zhang, J. Liu, W. Fan, L. Zhou, W. Peng, J. Shi, *Adv. Funct. Mater.*, 2013, **23**, 298-307.
40 A. Xia, M. Chen, Y. Gao, D. Wu, W. Feng, F. Li, *Biomaterials* 2012, **33**, 5394-5405.
41 H. Xing, W. Bu, Q. Ren, X. Zheng, M. Li, S. Zhang, H. Qu, Z. Wang, Y. Hua, K. Zhao, L. Zhou, W. Peng, J. Shi, *Biomaterials*, 2012, **33**, 5384-5393.
42 S. Zeng, M.-K. Tsang, C.-F. Chan, K.-L. Wong, J. Hao, *Biomaterials*, 2012, **33**, 9232- 9238.
43 C. Y. Lai, B. G. Trewyn, D. M. Jeftinija, K. Jeftinija, S. Xu, S. Jeftinija, V. S. Y. Lin, *J. Am. Chem. Soc.*, 2003, 125, 4451-4459.
44 J. A. Liu, W. B. Bu, L. M. Pan, J. L. Shi, *Angew. Chem.Int. Edit.*, 2013, **52**, 4375-4379.
45 P. Yang, S. Gai, J. Lin, *Chem. Soc. Rev.*, 2012, 41, 3679-3698.

46 M. Vallet-Regi, F. Balas, D. Arcos, *Angew. Chem. Int. Ed.*, 2007, **46**, 7548-7558.

47 Z. X. Li, J. C. Barnes, A. Bosoy, J. F. Stoddart, J. I. Zink, *Chem. Soc. Rev.*, 2012, **41**, 2590-2605.

48 Q. Zhan, J. Qian, H. Liang, G. Somesfalean, D. Wang, S. He, Z. Zhang, S. Andersson-Engels, *ACS Nano*, 2011, **5**, 3744-3757.

49 R. Weissleder, *Nat. Biotechnol.*, 2001, **19**, 316-317.

50 Z. Jiang, M. Xu, F. Li, Y. Yu, *J. Am. Chem. Soc.*, 2013, **135**, 16446-16453.

51 Y. T. Zhong, G. Tian, Z. J. Gu, Y. J. Yang, L. Gu, Y. L. Zhao, Y. Ma, J. N. Yao, *Adv. Mater.*, 2014, **26**, 2831-2837.

52 D. Wang, B. Xue, X. G. Kong, L. P. Tu, X. M. Liu, Y. L. Zhang, Y. L. Chang, Y. S. Luo H. Y. Zhao, H. Zhang, *Nanoscale*, 2015, **7**, 190-197.

53 Y. F. Wang, G. Y. Liu, L. D. Sun, J. W. Xiao, J. C. Zhou C. H. Yan, *ACS Nano*, 2013, **7**, 7200-7206.

54 X. Xie, N. Gao, R. Deng, Q. Sun, Q. Xu X. Liu, *J. Am. Chem. Soc.*, 2013, **135**, 12608-12611.

55 H. Wen, H. Zhu, X. Chen, T. F. Hung, B. Wang, G. Zhu, S. F. Yu F. Wang, *Angew. Chem. Int. Ed.*, 2013, **125**, 1-6.

56 J. P. Lai, Y. X. Zhang, N. Pasquale, K. B. Lee, *Angew. Chem. Int. Ed.*, 2014, **53**, 1-6.

57 Zhou, M.; Zhang, R.; Huang, M.; Lu, W.; Song, S.; Melancon, M. P.; Tian, M.; Liang, D.; Li, C. *J. Am. Chem. Soc.*, 2010, **132**, 15351-15358.X. J. Wang, C. Wang, L. Cheng, S. T. Lee, Z. Liu, *J. Am. Chem. Soc.*, 2012, 134, 7414-7422.

58 Y. Li, W. Lu, Q. Huang, C. Li, W. Chen, *Nanomedicine*, 2010, **5**, 1161-1171.

59 B. A. Dong, S. Xu, J. A. Sun, S. Bi, D. Li, X. Bai, Y. Wang, L. P. Wang, H. W. Song, *J. Mater. Chem.*, 2011, **21**, 6193-6200.

60 Q. W. Tian, J. Q. Hu, Y. H. Zhu, R. J. Zou; Z. G. Chen, S. P. Yang, R. W. Li, Q. Q. Su, Y. Han, X. G. Liu, *J. Am. Chem. Soc.*, 2013, **135**, 8571-8577.

61 L. Cheng, J. J. Liu, X. Gu, H. Gong, X. Z. Shi, T. Liu, C. Wang, X. Y. Wang, G. Liu, H. Y. Xing, W. B. Bu, B. Q. Sun, Z. Liu, *Adv. Mater.*, 2014, **26**, 1886-1893.

62 T. Liu, C. Wang, X. Gu, H. Gong, L. Cheng, X. Z. Shi, L. Z. Feng, B. Q. Sun, Z. Liu, *Adv. Mater.*, 2014, **26**, 3433-3440.

63 K. Dong, Z. Liu, Z. H. Li, J. S. Ren, X. G. Qu, *Adv. Mater.*, 2013, **25**, 4452-4458.

64 L. G. Guo, I. Panderi, D. D. Yan, K. Szulak, Y. J. Li, Y. T. Chen, H. Ma, D. B. Niesen, N. Seeram, A. Ahmed, B. F. Yan, D. Pantazatos, W. Lu, *ACS Nano*, 2013, **7**, 8780-8793.

65 J. Park, K. J. An, Y. S. Hwang, J. G. Park, H. J. Noh, J. Y. Kim, J. H. Park, N. M. Hwang, T. Hyeon, *Nat. Mater.*, 2004, **3**, 891-895.

66 C. Li, Z. Hou, Y. Dai, D. Yang, Z. Cheng, P. A. Ma, *J. Lin, Biomater. Sci.*, 2013, **1**, 213-223.

67 G. Wang, Q. Peng, Y. Li, *J. Am. Chem. Soc.* 2009, **131**, 14200-14201.

68 G. Y. Chen, T. Y. Ohulchanskyy, A. Kachynski, H. Ågren, P. N. Prasad, *ACS Nano.*, 2011, **5**, 4981-4986.

69 B. Shao, Q. Zhao, Y. Jia, W. Lv, M. Jiao, W. Lu, H. You, *Chem. Commun.*, 2014, **50**, 12706-12709.

70 L.-D. Sun, Y.-F. Wang, C.-H. Yan, *Acc. Chem. Res.*, 2014, **47**, 1001-1009.

71 J. Zhou, M. Yu, Y. Sun, X. Zhang, X. Zhu, Z. Wu, D. Wu, F. Li, *Biomaterials*, 2011, **32**, 1148-1156.